

Propagation of the First Flames in Type Ia Supernovae

M. Zingale

*Department of Physics and Astronomy, SUNY Stony Brook, Stony Brook, NY, 11794-3800,
USA*

`mzingale@mail.astro.sunysb.edu`

L. J. Dursi

*Canadian Institute for Theoretical Astrophysics, University of Toronto, Toronto, ON,
M5S 3H8, Canada*

`ljdursi@cita.utoronto.ca`

ABSTRACT

We consider the competition of the different physical processes that can affect the evolution of a flame bubble in a Type Ia supernovae — burning, turbulence and buoyancy. Even in the vigorously turbulent conditions of a convecting white dwarf, thermonuclear burning that begins at a point near the center (within 100 km) of the star is dominated by the spherical laminar expansion of the flame, until the burning region reaches kilometers in size. Consequently flames that ignite in the inner ≈ 20 km promptly burn through the center, and flame bubbles anywhere must grow quite large—indeed, resolvable by large-scale simulations of the global system—for significant motion or deformation occur. As a result, any hot-spot that successfully ignites into a flame can burn a significant amount of white dwarf material. This potentially increases the stochastic nature of the explosion compared to a scenario where a simmering progenitor can have small early hot-spots float harmlessly away. Further, the size where the laminar flame speed dominates other relevant velocities sets a characteristic scale for fragmentation of larger flame structures, as nothing—by definition—can easily break the burning region into smaller volumes. This makes possible the development of semi-analytic descriptions of the earliest phase of the propagation of burning in a Type Ia supernovae, which we present here. Our analysis is supported by fully resolved numerical simulations of flame bubbles.

Subject headings: supernovae: general — white dwarfs — hydrodynamics — nuclear reactions, nucleosynthesis, abundances — conduction — methods: numerical

1. INTRODUCTION

Numerical modeling of Type Ia supernovae (SNe Ia) has shown that a thermonuclear burning front propagating outward from the center of a carbon/oxygen white dwarf can release enough energy to unbind the star (see for example Röpke and Hillebrandt 2005; Gamezo et al. 2005). To prevent the overproduction of iron-group elements and allow for the necessary expansion of the white dwarf, this burning front must begin as a deflagration (Nomoto et al. 1976), but may later transition into a detonation (Niemeyer and Woosley 1997; Khokhlov et al. 1997). One of the greatest uncertainties in modeling SNe Ia lies in understanding the earliest stages of burning. Large-scale simulations seed the explosion with one or more physically large hot-spots. Variations in the number and location of these hot-spots can lead to a wide variety of different outcomes (Niemeyer et al. 1996; Plewa et al. 2004; García-Senz and Bravo 2005; Roepke et al. 2006).

Leading up to the explosion, accretion onto the surface of the white dwarf compresses the star and raises its central density and temperature. As the temperature increases, the carbon near the center can begin to fuse, releasing heat and driving convection throughout the star. This smoldering phase lasts for about a century (Wunsch and Woosley 2004). Numerical simulations have just begun to capture the dynamics of this phase (Höflich and Stein 2002; Kuhlen et al. 2006). Some models have shown that the central heating leads to a large scale dipole flow in the star (Kuhlen et al. 2006) which may favor off-center ignition. What we know for sure is that at the point of ignition, the white dwarf will be turbulent, and likely with typical intensities of 100 km s^{-1} on scales of 200 km (Woosley et al. 2004)

As the nuclear energy generation rate increases, eventually, hot plumes will develop whose cooling time (via expansion and neutrinos) is longer than the nuclear timescale, and a flame will be born (Woosley et al. 2004). Once ignited, the flame bubble will burn outward as it buoyantly rises, eventually wrinkling due to drag, the Rayleigh-Taylor instability, and interactions with turbulence generated from the convection. In this paper, we investigate the evolution of these very first flame ‘bubbles’. We look at the interplay between these physical processes to determine what size the bubble can grow to while remaining roughly spherical—this is the maximum size bubble that large scale calculations should use to initialize their explosion. We also are interested in the backward propagation of the flame and determining how off center a flame can begin such that buoyancy cannot carry it away faster than it burns through the center of the star. This will have important consequences for off-center ignition models.

Garcia-Senz and Woosley (1995) explored the evolution of buoyant plumes in the pre-ignition white dwarf and argued that multi-point, rather than single point ignition is more likely. Their results showed that the hot spots can travel great distances from the center

before igniting, and that this distance is relatively insensitive to the initial bubble size. Bychkov and Liberman (1995) described a picture of SNe Ia explosion in which the flame begins at multiple points near the center which quickly burn together. The resulting merged bubble has a higher terminal velocity and floats away from the center, leaving behind unburned carbon and oxygen at the center. They argue that this sets the stage for a detonation wave, ignited near the center, to burn through the star.

More recently, Iapichino et al. (2006) present a parameter study of two-dimensional smoldering bubbles in pre-ignition conditions in the white dwarf. They consider initial sizes in the range of 0.2 to 5 km at a range of initial distances from the center of the star. They conclude that larger bubbles are more likely to run away and that, in contrast to Garcia-Senz and Woosley (1995), the short timescale before these bubbles either ignite or disperse implies that the bubbles do not stray far from their origin. They attribute the disparity with the Garcia-Senz and Woosley (1995) results to multidimensional effects in the bubble evolution.

We concern ourselves with a slightly different problem—once a flame ignites at a point and begins burning outwards (a flame bubble), how does it evolve. This has seen very limited numerical work, mostly because of the difficulty in resolving the flame and evolving the state for long periods of time. Initial results of resolved bubbles in three-dimensions were presented in Zingale et al. (2005a). Here, we restrict our simulations to two dimensions, to allow for a range of different calculations to be carried out while resolving both the flame structure and the large-scale hydrodynamic motions. Since we consider only the onset of bubble distortion through hydrodynamic motions, two dimensional simulations are quite adequate.

In § 2, we present a semi-analytic model for the evolution of a flame bubble. Numerical simulations supporting this model are presented in § 3. Finally, in § 4, we discuss the implications of this flame bubble model on the ignition of Type Ia supernovae.

2. THE EVOLUTION OF A FLAME BUBBLE

We consider the evolution of a flame bubble by comparing the timescales of the physical processes that can affect the dynamics. For SNe Ia, these timescales are set by the laminar flame speed, S_l , the bubble rise velocity, v_b , and the turbulent intensity, v_{turb} , over scales of the size of the bubble and smaller. If the laminar flame speed exceeds all of the other velocities on the bubble scale, then we expect the bubble to remain mostly spherical in shape and expand in radius solely by burning outward.

For a spherical flame burning outward—or indeed burning in any geometry where the burned material is not free to move—the expansion of the material as it is burned causes the

bubble to expand at a rate greater than the laminar flame speed. The mass of fuel consumed in a time interval Δt is $4\pi R^2 \rho_{\text{fuel}} S_l \Delta t$, where R is the radius of the bubble. Across the burning front, the ash expands, pushing the radius of the bubble out at a speed \dot{R} . The ash mass formed over the time interval Δt is equal to the mass consumed, so

$$4\pi R^2 \rho_{\text{fuel}} S_l \Delta t = 4\pi R^2 \rho_{\text{ash}} \dot{R} \Delta t \quad (1)$$

Therefore, the expansion velocity of the bubble is

$$\dot{R} = \frac{\rho_{\text{fuel}}}{\rho_{\text{ash}}} S_l = \frac{1 + \text{At}}{1 - \text{At}} S_l \quad (2)$$

where $\text{At} = (\rho_{\text{fuel}} - \rho_{\text{ash}})/(\rho_{\text{fuel}} + \rho_{\text{ash}})$ is the Atwood number. The radius of the bubble would be given by

$$R(t) = R_0 + \frac{1 + \text{At}}{1 - \text{At}} S_l t . \quad (3)$$

Besides this ‘volume creation’ effect, geometry also comes in through the curvature and strain of the outgoing spherical flame. The curvature and strain of the flame ‘dilute’ heat transport outwards, decreasing the velocity of an outgoing spherical flame (*e.g.*, Dursi et al. 2003). This effect is only significant for bubbles sufficiently small (with respect to the flame thickness) that the curvature and strain are relatively large, typically tens of flame thicknesses. We will generally be considering flame bubbles of at least many thousands of flame thicknesses in radius, where this correction is completely unimportant; however we include it in the calculations here for consistency when we later consider very low density flames where the thickness is large enough that this effect is significant. The correction to the flame velocity is

$$S'_l = S_l (1 + \text{MaKa}) \quad (4)$$

where the Markstein number Ma for astrophysical flames is of order -1 (Dursi et al. 2003), and the dimensionless strain rate, given by the Karlovitz number Ka , is given for an expanding flame as

$$\text{Ka} = \frac{(d - 1) l_f}{R} \frac{\dot{R}}{S_l} \quad (5)$$

where $(d - 1) = 2$ for an expanding spherical flame, and 1 for an expanding flame ‘cylinder’. Including both the volume creation and curvature effects gives

$$\dot{R} = S_l \left(\frac{1 + \text{At}}{1 - \text{At}} \right) \left[1 - \text{Ma} \frac{l_f}{R} (d - 1) \left(\frac{1 + \text{At}}{1 - \text{At}} \right) \right]^{-1} \quad (6)$$

Competing against the simple expansion of the flame are the buoyancy caused by the density difference between the cold fuel and hot burned ash, and externally imposed turbulence from the centuries-long convective simmering which has occurred before the ignition of the first flames.

The buoyancy of the bubble causes the bubble both to rise, and to potentially be disrupted by the vortical motions generated by its own rising or Rayleigh-Taylor/Kelvin-Helmholtz instabilities (*e.g.*, Robinson et al. 2004; Iapichino et al. 2006). Buoyancy causes the burned material to accelerate upwards from the center of the white dwarf, however very quickly the bubble attains a (quasi-)steady terminal velocity set by the balance between gravitational acceleration and fluid drag.

In principle, obtaining this steady characteristic buoyant velocity is almost intractable, as the bubble will distort (in a velocity-dependent way) as it rises, greatly complicating the flow around the bubble. However, since we are interested in the case where the flame velocity is still nearly dominant, we expect the flame bubble to remain essentially spherical. In this limit there is extensive theoretical work (*e.g.*, Harper 1972; Magnaudet and Eames 2000) both past and ongoing (*e.g.*, Joseph 2003). Such work generally considers terrestrial fluids, where the gravitational acceleration is spatially constant, and fluid properties do not change over the scale of the bubble. For the analysis considered here, we will make the same assumptions; in a white dwarf, the typical pressure scale height is something like 200 km—as we will show later, we are mostly concerned with bubbles that are $\lesssim 1$ km, so changes in gravity or fluid state variables across the size of the bubble are not expected to be important.

In the case of a bubble rising in a quiescent medium, the drag is due to the wake behind the bubble as it rises. A gas bubble (*e.g.*, one where the bubble density is negligible) in an incompressible, inviscid fluid, has been shown to be well approximated by a rigid rising spherical bubble of negligible velocity, leading to a rise velocity of (Davies and Taylor 1950)

$$v_{b,DT} = \frac{2}{3} \sqrt{gR} \quad (7)$$

where g is the local gravitational acceleration and R is the radius of the spherical bubble. In the case of a two-dimensional bubble (eg, a rising cylinder), consideration of the potential flow over a cylinder rather than a sphere gives a numerical prefactor of 1/2 rather than 2/3.

In the case of non-zero bubble density (*e.g.*, non-unity Atwood number), the rising bubble will not ‘feel’ the full gravitational acceleration. Recently, a result has been derived (Goncharov 2002) for a related case, that of the Rayleigh-Taylor instability, which has been used in this context by Iapichino et al. (2006):

$$v_{b,RT} = \sqrt{\frac{2At}{At + 1} \frac{gR}{2\pi}}. \quad (8)$$

The combination of the terms $2At/(At + 1)g$ can be thought of as an effective gravity, where $2At/(At + 1) = \delta\rho/\rho_{\text{ambient}}$. However, while this correctly takes into account the density ratio, because of the different geometry being considered in the Rayleigh-Taylor instability,

the numerical factor is inapplicable to the rising bubble case (that is, in the limit $\text{At} \rightarrow 1$, this expression is off by a factor of $(2/3)\sqrt{2\pi} \approx 1.67$).

A simpler expression one sometimes sees in the literature takes the form of the Davies and Taylor results and sets $g \rightarrow \text{At}g$

$$v_{b,\text{DT+A}} = \sqrt{\text{At}gR} . \quad (9)$$

This fails to capture the bubble motion in two respects—the incorrect $\text{At} \rightarrow 1$ limit, and an incorrect scaling with At .

A further correction is due to the fact that our bubbles are expanding as they rise. Taking this into account (*e.g.*, Ohl et al. 2003), together with the above correction for effective gravity on the bubble, we have

$$v_{b,\text{rise}} = \frac{d+1}{6} \left(\sqrt{\frac{2\text{At}}{\text{At}+1} gR + \left(\frac{(d-1)\dot{R}}{4} \right)^2} - \frac{(d-1)\dot{R}}{4} \right) . \quad (10)$$

Here $d = 3$ for a spherical bubble and $d = 2$ for a 2d flame ‘cylinder’, and \dot{R} is given by Eq. 6. Note that, all else being equal, expansion of the bubble acts to reduce the rising terminal velocity.

As we see from the R -dependence of Eq. 10, for larger and larger bubbles, the buoyancy increasingly outweighs any fluid drag on the bubble, and rise velocity grows. When the rise velocity exceeds the speed of the laminar flame, we would expect the shear on the sides and the vorticity generation behind the bubble to start to play a role in the bubble evolution. In particular, the bubble should begin to roll up. We note that this is also the point where the Rayleigh-Taylor instability will set in, as equating the bubble rise speed to the laminar speed yields the fire-polishing length (Timmes and Woosley 1992), although typically large-scale bubble distortions due to the bubble’s own motion will occur first (Robinson et al. 2004).

These bubble rise velocities are plotted as a function of the bubble sizes in Fig. 1 for the specific case of a $d = 2$ cylindrical bubble burning into a material of $\rho = 4 \times 10^9 \text{ g cm}^{-3}$ in a gravitational field of $g = 10^{10} \text{ cm s}^{-2}$, along with results of a multidimensional hydrodynamical simulation (described in §3) for comparison. We use $v_{b,\text{rise}}$ as the fiducial laminar bubble rise velocity for the rest of this paper.

In a turbulent medium, another source of drag exists beyond that created in the wake of the rising bubble—a ‘turbulent eddy viscosity’. In the regime where this ‘viscosity’ dominates, the rise velocity coming from balancing the viscous drag for a sphere and the buoyant

force gives (Moore 1959)

$$v_{b,\text{visc}} = \frac{1}{6} \frac{gR^2}{\nu_{\text{turb}}} = \frac{1}{12} \frac{gR}{v_{\text{turb},b}} \quad (11)$$

where the turbulent eddy viscosity on the scale of the bubble is assumed to be $\nu_{\text{turb}} = 2Rv_{\text{turb},b}$ where $v_{\text{turb},b}$ is the turbulent velocity on the bubble scale. We will use the same correction for effective gravity as above.

Assuming Kolmogorov turbulence, for which there is some evidence in this context (Zingale et al. 2005b; Cabot and Cook 2006), the characteristic turbulent velocity on the bubble scale, $(2R)$, is

$$v_{\text{turb},b} = V \left(\frac{2R}{L} \right)^{1/3} \quad (12)$$

where V is the turbulent intensity on the integral scale L . The corresponding velocity on the flame scale is

$$v_{\text{turb},f} = V \left(\frac{l_f}{L} \right)^{1/3} = \left(\frac{l_f}{2R} \right)^{1/3} v_{\text{turb},b}. \quad (13)$$

Throughout this work we will assume characteristic values for $V \approx 100 \text{ km s}^{-1}$ on scales $L \approx 200 \text{ km}$, consistent with, *e.g.* Höflich and Stein (2002) and Kuhlen et al. (2006).

In general, we expect the turbulent ‘viscous’ drag on the bubble to dominate for sufficiently small bubbles, and the drag produced by wake of the bubble itself to dominate for larger bubbles. The ‘viscous’ drag dominates if the viscous drag velocity prevents the bubble from rising as it would without the turbulent viscosity, $v_{b,\text{visc}} < v_{b,\text{rise}}$. Ignoring, for the time being, the effect of flame speed driven expansion on the rise velocity of the bubbles, this happens on scales

$$R < 2621.44 \text{ cm} \left(\frac{\text{At} + 1}{2\text{At}} \right)^3 \frac{(V/100 \text{ km s}^{-1})^6}{(g/10^{10} \text{ cm s}^{-2})^3 (L/200 \text{ km})^2} \quad (14)$$

which, for typical values of At of 0.11, gives $R \approx 3.4 \text{ km}$.

As long as the flame speed dominates the rise velocities, the evolution of the flame bubble will consist solely of the spherical expansion of the flame as smaller disturbances are burned out. As the bubble grows, the rise velocity also increases, leading to distortion of the sphericity of the bubble; a ‘mushroom cap’ forms caused by the vortical motions induced by the bubbles own rise. We refer to the radius at which the flame speed is no longer dominant as the distortion radius, R_d .

Beyond its effect on the rise velocity, the turbulent velocity field in the white dwarf on scales equal to or lesser than the bubble size can also directly distort the bubble. (In the extreme case that even the turbulent velocity on the scale of the flame thickness exceeds the

flame velocity, it can directly affect the burning, leading to the transition to the distributed burning regime (Niemeyer and Woosley 1997; Niemeyer and Kerstein 1997; Bell et al. 2004)).

If the velocity of turbulent eddies of the size of the bubble is smaller than the flame speed, then the flame will burn through these, and little deformation will occur. As with buoyancy, however, as the bubble increases in size, the turbulent velocities on the scale of the bubble become larger and larger, and eventually they will begin to affect the dynamics of the bubble. This only happens on larger scales, however; because in the case we are considering the flame velocity is larger than the buoyant velocity, the turbulence can effect the slower buoyant rise speed before it can affect the faster-moving geometry of the flame bubble itself. Thus the distortion due to buoyant motions will occur first, and we need not consider direct turbulent distortion of the flame bubble here.

Equating the viscous bubble terminal velocity in Eq. 11 with the laminar burning speed of the flame bubble in Eq. 6, we arrive at an expression for the maximum radius of a bubble before deformation sets in due to buoyant motions

$$R_d \approx 3.9 \times 10^4 \text{ cm} \left(\frac{(1 + \text{At})^2}{2\text{At}(1 - \text{At})} \right)^{3/2} \left(\frac{(V/100 \text{ km s}^{-1})^3 (S_l/100 \text{ km s}^{-1})^3}{(g/10^{10} \text{ cm s}^{-2})^3 (L/200 \text{ km})} \right)^{1/2} \quad (15)$$

or $R \approx 6.2 \text{ km}$ for $\text{At} = 0.11$. We can do a little better than this by examining the behavior as a function of density. For the white dwarf model considered here, gravity is well fit (to within 5% between densities of $5 \times 10^8 \text{ g cm}^{-3}$ and $2 \times 10^9 \text{ g cm}^{-3}$) by

$$g(\rho) = 1.198 \times 10^{10} \text{ cm s}^{-2} \sqrt{(2.6269 - \rho_9)(\rho_9 + 0.860752)}. \quad (16)$$

The properties of the flame from Timmes and Woosley (1992) are given in a fit provided in that paper,

$$S_l = 92 \times 10^5 \text{ cm s}^{-1} \left(\frac{\rho}{2 \times 10^9 \text{ g cm}^{-3}} \right)^{0.805} \left(\frac{X(^{12}\text{C})}{0.5} \right)^{0.889} \quad (17)$$

however, we used this modified version of that flame speed which fits better at lower densities at the cost of some accuracy at higher densities:

$$S_l = \frac{1}{2} \left(92 \left(\frac{\rho_9}{2} \right)^{0.805} \left(\frac{X(^{12}\text{C})}{0.5} \right)^{0.889} + 53.5 \left(\frac{\rho_9}{2} \right)^{1.318} \left(\frac{X(^{12}\text{C})}{0.5} \right)^{1.132} \right) \text{ km s}^{-1} \quad (18)$$

and we compute a similar fit for the Atwood number computed from the data tabulated in that paper,

$$\text{At} = 0.114 \rho_9^{-0.3233} X(^{12}\text{C})^{0.0479} \quad (19)$$

where $\rho_9 = \rho/10^9 \text{ g cm}^{-3}$ and $X(^{12}\text{C})$ is the mass fraction of carbon.

Substituting these results into Eq. 15, and expanding in a power series in $\log(\rho_9)$ and $\log(X(^{12}\text{C}))$ around a relevant density $\rho_9 = 1.5$ and $X(^{12}\text{C}) = 0.3$ where all of the fits are particularly good, and neglecting an additional very weak dependence on $X(^{12}\text{C})$, one finds

$$R \approx 32.5 \text{ cm} \left(\frac{\rho_9}{0.1} \right)^{2.32} \left(\frac{X(^{12}\text{C})}{0.3} \right)^{1.30} \left(\frac{V}{100 \text{ km s}^{-1}} \right)^{3/2} \left(\frac{L}{200 \text{ km}} \right)^{-1/2}. \quad (20)$$

If one instead considers the self-drag rather than the viscous drag, and follows the same procedure but with V given by Eq. 10 one finds

$$R \approx 24.2 \text{ cm} \left(\frac{\rho_9}{0.1} \right)^{2.44} \left(\frac{X(^{12}\text{C})}{0.3} \right)^{1.88}. \quad (21)$$

Figure 3 shows this maximum radius where the ‘viscous’ rise speed becomes equal to the flame speed as a function of density, both from semi-analytically comparing the velocities as in Fig. 2, and from the expression given in Eq. 20. The plot also shows the transition from the rise velocity being dominated by turbulent eddies to that of the bubbles own motion at $\rho \approx 2 \times 10^8 \text{ g cm}^{-3}$.

For concreteness, we consider these velocities given in Eqs. 6, 10, 11, 12, and 13 with the gravitational acceleration as a function of density taken from a pre-ignition Chandrasekhar white dwarf model produced with the Kepler code (Weaver et al. 1978) with a central density of $2.6 \times 10^9 \text{ g cm}^{-3}$, a central temperature of $7 \times 10^8 \text{ K}$, and a carbon abundance by mass of 0.3. Since the flame thickness varies considerably over the range of densities we examine, we measure the bubble radius in units of the laminar flame thermal thickness. The laminar flame properties—flame speed and Atwood number—are taken from Timmes and Woosley (1992), and logarithmically interpolated between tabulated points. Figure 2 shows the intersections of these different physical processes for bubbles with radii of 5, 500, 5×10^4 , and $5 \times 10^6 l_f$.

As we see, for small bubbles ($R = 5 l_f$), the laminar burning speed dominates over the turbulence and the buoyancy for all densities greater than $\sim 8 \times 10^7 \text{ g cm}^{-3}$. As the bubble gets bigger, the density below which laminar burning no longer dominates increases. For a bubble of radius $500 l_f$, the crossover point is about $1.5 \times 10^8 \text{ g cm}^{-3}$. For a $5 \times 10^4 l_f$ bubble, it is $3 \times 10^8 \text{ g cm}^{-3}$, and for a $5 \times 10^6 l_f$ bubble, it is $8 \times 10^8 \text{ g cm}^{-3}$.

Clearly, at high densities, such as those of the ignition conditions, the bubbles can grow to enormous sizes (compared to the flame width) without feeling the effects of turbulence or buoyancy. As the panel for a $5 \times 10^6 l_f$ bubble shows, once the bubble is large enough, it is the buoyancy effects that will be felt first. This further suggests understanding the dynamics of flame bubbles is important to understanding the propagation of the very first flames in SNe Ia.

The previous discussion assumes a quasi-static flame bubble, considered at different sizes and positions/densities. The dynamic case, where the bubble expands and rises, is in principle much more complicated, but if we restrict ourselves to considering where the bubble is dominated by flame expansion, the picture greatly simplifies, as we see in Fig. 4. Here, we look at the evolution of individual bubbles with a variety of starting points and ‘evolve’ the flame bubble in simple semi-analytic way—the size increases with laminar burning speed (Eq. 6) and the position increases with buoyancy, assumed (as an upper limit) to be the minimum of the terminal rise velocities given above in Eqs. 11 and 10. We stop evolution when buoyancy speed exceeds flame speed, where we expect the bubble to start becoming distorted. As we see, because (by construction) the bubbles rise velocity is small, the ‘evolution’ consists simply of the bubble expanding to the critical size where rise velocity begins to compete with the flame velocity. Thus one can greatly simplify consideration of rising flame bubbles in high-density regions by ignoring hydrodynamical effects until they reach the size given by Eq. 20. A similar analysis was explored in Garcia-Senz and Woosley (1995) for igniting hot spots.

Whether or not a flame burns through the center of the white dwarf can determine the importance of an off-center ignition (*e.g.*, Plewa et al. 2004; Roepke et al. 2006), and can determine whether a central ‘pool’ of unburned fuel remains for possible later burning. Certainly if the undistorted bubble can expand to a size greater than its initial radial position from the center of the star, then it will both consume the fuel center of the star and proceed in more symmetric fashion. In Fig. 5, we consider the evolution of bubbles that initially begin with radii of 10 flame thicknesses and burn outwards. If the bubble begins sufficiently close to the center of the star—for the density structure of the progenitor considered here, within $\approx 23.5\text{km}$ —the flame will pass through the center. Woosley (2001) used similar arguments to show that the minimum separation of bubbles so that they do not merge as they float is about 5 km. Woosley (2005) used a simpler estimate of the terminal velocity of the bubble to estimate that the radius beyond which bubbles do not burn through the center is 20-40 km. This radius is sensitive to the central density of the white dwarf.

3. NUMERICAL MODEL

To test the ideas proposed above—and in particular the quantitative predictions of laminar expansion until buoyancy effects become important—we perform hydrodynamical simulations of burning, buoyant, flame bubbles. We use a low Mach hydrodynamics code (Bell et al. 2004) to follow the evolution. Here, the sound waves are filtered out of the system, allowing us to take much larger timesteps than a fully compressible code. A second-

order accurate approximate projection method is used to evolve the state. This code has been applied to both terrestrial (Bell et al. 2005) and astrophysical flames (Bell et al. 2004; Zingale et al. 2005b). Since the laminar flames we are dealing with all have Mach numbers $< 10^{-3}$, this is a very good approximation.

We resolve the thermal thickness of the flame and track the dynamics of the bubble without the need for a flame model. Resolution studies with this code have shown us that we need about 5 zones in the thermal thickness of the flame to accurately capture the burning. A single $^{12}\text{C} + ^{12}\text{C}$ reaction rate is used, with the energy release corresponding to ^{24}Mg production. The rate is modified to include screening (using the screening routine from the Kepler code, Weaver et al. 1978)—this leads to slightly higher flame speeds than reported in earlier works (see e.g. Bell et al. 2004). Finally, we use a general equation of state allowing for arbitrary degeneracy and degrees of relativity (Timmes and Swesty 2000), and the conductivities described in Timmes (2000). Table 1 lists the properties of planar laminar flames with this input physics. Resolving the flame restricts us to bubbles of small size ($< 1000 l_f$). However, by following bubbles in the flamelet regime, we expect that the results we find will scale to bubbles of large size, with similar Froude numbers. Our boundary conditions are outflow on the top and sides and slip-wall on the bottom. We note that these calculations are only used to test our ideas about the deformation radius of a flame bubble—we do not use these specific flame parameters in the semi-analytic estimates presented above. There, we use only the results presented in Timmes and Woosley (1992).

We will follow the evolution of bubbles at different densities—and thus with different balances between flame speed and buoyancy—to get a feel for how the evolution unfolds and verify the analytic description sketched out above. The simulations presented here are all two-dimensional, using a Cartesian geometry. Previously, we looked at three-dimensional flame bubbles (Zingale et al. 2005a), but the range of length scales we need to resolve for a range of densities make a three-dimensional study infeasible. While axisymmetric calculations would capture the three-dimensional volume factors, the Cartesian geometry used here should give qualitatively the same behavior to the point of roll-up (e.g., Robinson et al. 2004). We do not consider externally-imposed turbulence in these simulations, as at these densities and scales the turbulence would swamp the effect we are trying to measure.

Figure 6 shows the expected cross over points for where we expect buoyancy to dominate over the laminar burning for three fuel densities, 4.0, 3.0, and $2.35 \times 10^7 \text{ g cm}^{-3}$, assuming 50% carbon / 50% oxygen. These plots were generated using the same method as Fig. 2, but considering fixed density and gravity and varying the flame bubble size. Flame properties (propagation speed and Atwood numbers) were interpolated from the values tabulated in Table 1. Turbulent velocities are shown for reference, but only the terminal rise velocity from

the bubbles own motions are shown. In these plots, as in Fig. 2, the laminar flame speed includes the Atwood number correction from Eq. 3 and the curvature correction from Eq. 4; because we are looking at larger flame thicknesses at these lower densities, the curvature correction is apparent in the variation of flame speed with bubble size.

Figure 7 shows the evolution of a flame bubble with a fuel density of $4 \times 10^7 \text{ g cm}^{-3}$. With our input physics, the laminar flame speed is $7.64 \times 10^4 \text{ cm s}^{-1}$ and the thermal thickness is 0.039 cm. The calculation was started by mapping a steady state laminar flame in a circular fashion onto the grid, with an initial radius of $6.4 l_f$. Adaptive mesh refinement was used to follow the flame. The finest level of refinement corresponds to a grid of 16384×32768 zones (or 5 zones / l_f). The domain is 128×256 cm in physical extent. As the figure shows, initially, the flame simply burns outward, staying roughly circular. Only when it reaches a radius of $\sim 500 l_f$ do we see significant deformation. At this point, the bubble would continue to roll up, but we stop the calculation, since the bubble is starting to take up a considerable fraction of the domain width.

The position of the bubble, its radius, rise velocity, and ash mass are shown in Figure 8. The top left panel shows the location of the topmost and bottommost extent of the bubble and the center of mass. The extrema are computed by laterally averaging the ash mass fraction and looking for the height where it exceeds 0.001. The center of mass is computed simply as

$$y_{\text{CM}} = \frac{\sum_{i,j} y_j \rho_{i,j} A_{i,j} X^{(24\text{Mg})}_{i,j}}{\sum_{i,j} \rho_{i,j} A_{i,j} X^{(24\text{Mg})}_{i,j}} \quad (22)$$

Here, the sum is over all the zones in the domain. $A_{i,j}$ is the area of the zone ($\Delta x \Delta y$), $\rho_{i,j}$ is the mass density of that zone, $X^{(24\text{Mg})}_{i,j}$ is the mass fraction of ash in the zone, and y_j is the vertical coordinate of the zone. The top right panel shows the radius of the bubble. This is taken to be half the distance between the left and right extrema of the ash, computed as described above. This is more properly a width of the bubble. This will be the true radius for the initial evolution of the bubble, when it is circular. As the bubble deforms, this is actually a measure of the cross-sectional radius of the bubble. The bottom left panel shows the velocity of the center of mass at timelevel n , v^n . This is computed via centered differencing of the center of mass position at the points we output plot files. Finally, the ash mass, shown in the bottom right panel, is computed as

$$M = \sum_{i,j} \rho_{i,j} A_{i,j} X^{(24\text{Mg})}_{i,j} \quad (23)$$

Since these are two-dimensional simulations, this has units of g cm^{-1} .

As we see, for the first 10^{-4} s, the bubble is expanding, and the downward flame propagation is faster than the rise velocity of the bubble. Then the bubble rise velocity becomes

equal to the laminar flame speed, and the ash region no longer reaches lower heights. For most of the evolution of the bubble, the radius expands according to Eq. 3, as expected when the buoyancy effects are negligible. The velocity of the bubble steadily rises through the course of the simulation, staying very close to the predicted terminal velocity (Eq. [10]) for the initial evolution. Since the bubble starts from rest and is continually accelerating, the velocity curve should not lie directly on top of the terminal velocity curve. Only at very late times, when the bubble is no longer spherical, does the rise velocity from the simulation overtaking our prediction. The mass plot shows that the total mass of the bubble increases by $4500\times$ over the simulation, showing the dominance of the burning at this density. We stop the simulation once the bubble grows to more than half the width of the domain to prevent any influence from the boundaries.

At 3×10^7 g cm $^{-3}$, the evolution proceeds in much the same fashion (Figure 9). Because the flame speed is lower ($S_l = 4.34 \times 10^4$ cm s $^{-1}$), we expect that the bubble will begin to roll up at a smaller radius. This simulation was run in a domain 192×256 cm large, with an effective grid of 12288×16384 zones (or 5 zones / l_f). The steady state flame was mapped onto the grid with an initial radius of $4.1 l_f$. As the figure shows, the bubble burns radially outward until it grows to a radius of $\sim 100 l_f$. At this point, it begins to deform. The integral quantities (Figure 10 again show the flame initially propagating downward until the rise velocity exceeds the laminar flame speed. We also again see that our prediction of the bubble velocity again agrees with the simulation to the point where the bubble begins to roll up.

Figure 11 shows the evolution of our lowest density bubble (fuel density of 2.35×10^7 g cm $^{-3}$). The laminar flame speed is roughly 3× lower ($S_l = 2.58 \times 10^4$ g cm $^{-3}$) and the flame thickness is $l_f = 0.18$ cm. The domain size is 160×320 cm, with an effective grid of 4096×8192 zones. The flame solution was mapped onto the grid with an initial radius of $8.8 l_f$. As discussed above, we expect this bubble to roll up at a much smaller radius. As the figure shows, already at a radius of $30 l_f$, the bubble is deforming.

The position, radius, velocity, and mass for the 2.35×10^7 g cm $^{-3}$ bubble are shown in Figure 12. As we see, the bubble quickly inflates in the very earliest moments, as the planar flame used to initialize the flame settles into the circular configuration. For the first $5 - 6 \times 10^{-5}$ seconds of evolution, the radius evolution parallels the theoretical prediction. It then gradually begins to diverge as the bubble begins to roll up. The buoyant velocity of the bubble quickly exceeds the prediction (Eq [10]), but levels off and stays roughly $1.25 - 1.5 \times$ higher for the remainder of the evolution. The mass increases by almost $120\times$ through the course of evolution.

The low density calculation was run at a resolution corresponding to 4.6 zones in the

thermal flame thickness. To test the sensitivity of our results, we performed a convergence study. Figure 13 shows the bubble velocity and mass as a function of time for four different resolutions, corresponding to $l_f/\Delta x$ of 1.15, 2.3, 4.6, and 9.2. As we see, the three highest resolution curves track each other very well, indicating that our simulations have converged. Only the very lowest resolution run shows a significant divergence, producing about 20% less ash than the converged solution. This is the result of under resolving the flame.

Figure 14 shows the carbon destruction rate ($-dX(^{12}\text{C})/dt$) for the $2.35 \times 10^7 \text{ g cm}^{-3}$ bubble at 10^{-4} s for the high-resolution run. A planar laminar flame has a peak carbon destruction rate of $-1.3 \times 10^5 \text{ s}^{-1}$. We see that the shear at the top of the bubble suppresses the burning rate slightly, while the cusp near the bottom of the bubble has a significantly higher burning rate. The flow field is represented by the vectors superposed on the rate. We see that below the bubble, the flow is carrying fuel toward the flame while above it, the flow is carrying fuel away from the flame. This flow pattern is similar to that seen in Zingale et al. (2005a), where a lower density flame bubble was evolved in three-dimensions. There, the flow managed to punch a hole through the top of the bubble, transforming it into a torus.

To within constants of order unity, the cross over point predicted in the analysis in § 2 seems to agree with the numerical results. In our two higher density bubbles, we had an extended period where the bubble stayed roughly spherical, and the rise velocity showed excellent agreement with our theoretical prediction, Eq. 10. This suggests that this picture can safely be extended to the ignition conditions, to allow us to make predictions about the evolution of the very first flame bubbles.

4. DISCUSSION

We presented a model for the early evolution of flame bubbles. Several functional forms for the terminal velocity of flame bubbles were explored. Our analysis was supported by resolved numerical simulations of flame bubbles at a range of densities. We showed that for initial flame bubbles at densities of $\rho_9 \gtrsim 2$ (eg, the inner $\approx 250\text{km}$ of the white dwarf) the laminar flame speed dominates other motions at least until the flame bubble approaches on order a half kilometer in size. This distance from the center is comparable to that explored in a recent study of off-center ignition (Roepke et al. 2006). A bubble at the very center of the star ($\rho_9 = 2.6$) will deform once it reaches a radius of 1 km. This suggests an (approachable) minimum resolution to capture all of the early bubble dynamics in large-scale simulations is on the order of a tenth of a kilometer. For comparison, the current state of the art explosion models (e.g. Röpke and Hillebrandt 2005) seed initial flame bubbles with radii

of a few kilometers with a resolution of 1 km, so they are just able to resolve the relevant lengthscales for a bubble ignited precisely at the center (by putting only 2 zones across the entire bubble).

These results further suggest a minimum size to which turbulent fragmentation can shred a burning region. For instance, in Iapichino et al. (2006), where a non-burning bubble is simulated, the turbulent motions dominate and it is suggested that this will continue to the smallest scales on which a flame can be ignited. However, the results presented here imply that had flame physics been included in those simulations the cross-over point between the turbulent speeds and flame speeds would have been well-resolved, and fragmentation would have ended on the scale of hundreds of meters, rather than tens of centimeters.

The existence of a (high) minimum scale to fragmentation places a limit on the burning rate of the initial rising burning region. If a burning region of volume \mathcal{V} is continuously fragmented into near-spheres of radius R_f , then the total surface area available for burning is $3\mathcal{V}/R_f$ and the burning rate is

$$\frac{d\mathcal{V}}{dt} = \left(\frac{3\mathcal{V}}{R_f} \right) \dot{R}. \quad (24)$$

Using our simple fits for $R_f(\rho)$ and $S_l(\rho)$, neglecting the At number effect as small $< 25\%$ at high densities, and assuming that we are dealing with large enough regions that flame curvature effects are small, we have a burning law

$$\frac{\dot{\mathcal{V}}}{\mathcal{V}} = 1.64 \times 10^4 \text{ sec}^{-1} \rho_8^{-1.335} \left(\frac{V}{100 \text{ km s}^{-1}} \right)^{-3/2} \left(\frac{L}{200 \text{ km}} \right)^{1/2} \left(\frac{X(^{12}\text{C})}{0.3} \right)^{-0.441} \quad (25)$$

Note that this is a different picture from the usual ‘turbulent flamelet’ sort of burning model, based on simulations such as Khokhlov (1995). In that paper, fragmentation was suppressed both by the geometry (a planar flame front, externally imposed by symmetry, so that on the largest modes fragmentation was suppressed) and the extremely thick model flame (so that only a few flame thicknesses fit in the box, and only the largest scales if even those could fragment).

In the turbulent flamelet picture, it is explicitly assumed there is a large separation of scales between that of the buoyant plume and the flame thickness, so that the flame can be greatly wrinkled without altering the overall geometry of the burning. This certainly seems to be a reasonable picture at large- to intermediate- densities ($\rho \gtrsim 5 \times 10^8 \text{ g cm}^{-3}$) where the typical fragment size would be tens or hundreds of thousands of flame thicknesses.

However, in non-planar, ‘rising bubble’ geometries it is seen that if a bubble can fragment, it does, on roughly the time it takes to rise one bubble height (Robinson et al. 2004; Iapichino et al. 2006). At high densities this would happen very slowly, as bubbles are large

and rise velocities are small. However, considering Fig. 3, we see that for lower densities ($\rho \lesssim 2 \times 10^8 \text{ g cm}^{-3}$), the typical fragment size would be hundreds of flame thicknesses or less, in which case fragmentation would quickly outstrip wrinkling as a method of producing burning surface area, producing a rapid increase in burning at an interesting density for reproducing observables in Type Ia supernovae. This will all happen on scales much smaller than those resolvable by multidimensional simulations. Verifying this new burning mechanism will require three-dimensional simulations to investigate fragmentation.

Another refinement to our model would be to include some stochastic advection, which changes not only the flame position, but more importantly the burning conditions—flame speed and local gravity. In particular, this would affect the radius at which ignited bubbles are guaranteed to burn through the center. Numerical simulations of the convective phase of SNe Ia have shown that large scale motions can exist. These can carry the flame bubbles far away from their initial location, affecting the results presented here.

We thank S.E. Woosley for providing the 1D models of the white dwarf used in this study and for many helpful discussions. We thank John Bell for help with the simulations and for useful feedback on the manuscript. We also thank Alan Calder for a thorough read of the manuscript and many helpful comments. Finally we thank Mike Lijewski for help with the simulation code. LJD acknowledges the support of the National Science and Engineering Research Council during this work. MZ acknowledges support from the Dept. of Energy, Office of Nuclear Physics Outstanding Junior Investigator award, DE-FG02-06ER41448. This work made use of NASA’s Astrophysical Data System. This research used resources of the National Center for Computational Sciences at Oak Ridge National Laboratory, which is supported by the Office of Science of the U.S. Department of Energy under Contract No. DE-AC05-00OR22725.

Table 1. Properties of planar simplified $^{12}\text{C} + ^{12}\text{C} \rightarrow ^{24}\text{Mg}$ flames into given fuel conditions.

ρ^a $\times 10^7 \text{ g cm}^{-3}$	$X(^{12}\text{C})$	S_l cm s^{-1}	l_f^b cm	At^c
2.35	0.5	2.58×10^4	0.18	0.241
3.0	0.5	4.34×10^4	0.078	0.224
4.0	0.5	7.63×10^4	0.039	0.205

^aDensity of fuel in units of 10^7 g cm^{-3} .

^bFlame thermal thickness, $l_f = (T_{\text{ash}} - T_{\text{fuel}}) / \max\{\nabla T\}$.

^c $\text{At} = (\rho_{\text{fuel}} - \rho_{\text{ash}}) / (\rho_{\text{fuel}} + \rho_{\text{ash}})$.

REFERENCES

J. B. Bell, M. S. Day, C. A. Rendleman, S. E. Woosley, and M. Zingale. Direct Numerical Simulations of Type Ia Supernovae Flames. II. The Rayleigh-Taylor Instability. *ApJ*, 608:883–906, June 2004. doi: 10.1086/420841.

J. B. Bell, M. S. Day, C. A. Rendleman, S. E. Woosley, and M. A. Zingale. Adaptive low Mach number simulations of nuclear flame microphysics. *Journal of Computational Physics*, 195(2):677–694, 2004.

J. B. Bell, M. S. Day, I. G. Shepherd, M. R. Johnson, R. K. Cheng, J. F. Grcar, V. E. Beckner, and M. J. Lijewski. Numerical simulation of a laboratory-scale turbulent V-flame. *Proc. Natl. Acad. Sci.*, 102(29):10006–10011, 2005.

V. V. Bychkov and M. A. Liberman. On the theory of Type IA supernova events. *A&A*, 304:440–+, December 1995.

W. H. Cabot and A. W. Cook. Reynolds number effects on Rayleigh-Taylor instability with possible implications for type Ia supernovae. *Nature Physics*, 2:562–568, August 2006. doi: 10.1038/nphys361.

R. M. Davies and Geoffrey Taylor. The mechanics of large bubbles rising through extended liquids and through liquids in tubes. *Proceedings of the Royal Society of London. Series A, Mathematical and Physical Sciences*, 200(1062):375–390, February 1950.

L. J. Dursi, M. Zingale, A. C. Calder, B. Fryxell, F. X. Timmes, N. Vladimirova, R. Rosner, A. Caceres, D. Q. Lamb, K. Olson, P. M. Ricker, K. Riley, A. Siegel, and J. W. Truran. The response of astrophysical thermonuclear flames to curvature and stretch. *ApJ*, 595(2):955–979, October 2003.

V. N. Gamezo, A. M. Khokhlov, and E. S. Oran. Three-dimensional Delayed-Detonation Model of Type Ia Supernovae. *Astrophysical Journal*, 623:337–346, April 2005. doi: 10.1086/428767.

D. García-Senz and E. Bravo. Type Ia Supernova models arising from different distributions of igniting points. *Astronomy and Astrophysics*, 430:585–602, February 2005. doi: 10.1051/0004-6361:20041628.

D. Garcia-Senz and S. E. Woosley. Type IA Supernovae: The Flame Is Born. *ApJ*, 454: 895–+, December 1995. doi: 10.1086/176542.

V. N. Goncharov. Analytical Model of Nonlinear, Single-Mode, Classical Rayleigh-Taylor Instability at Arbitrary Atwood Numbers. *Physical Review Letters*, 88(13):134502–+, April 2002. doi: 10.1103/PhysRevLett.88.134502.

P. Höflich and J. Stein. On the thermonuclear runaway in Type Ia supernovae: How to run away? *Astrophysical Journal*, 568:779–790, April 2002.

J. F. Harper. The motion of bubbles and drops through liquids. *Adv. Appl. Mech*, 12:59–129, 1972.

L. Iapichino, M. Brüggen, W. Hillebrandt, and J. C. Niemeyer. The ignition of thermonuclear flames in type Ia supernovae. *A&A*, 450:655–666, May 2006. doi: 10.1051/0004-6361:20054052.

Daniel D. Joseph. Rise velocity of a spherical cap bubble. *J. Fluid Mech.*, 488:213–223, 2003. doi: 10.1017/S0022112003004968.

A. M. Khokhlov. Propagation of Turbulent Flames in Supernovae. *ApJ*, 449:695–+, August 1995. doi: 10.1086/176091.

A. M. Khokhlov, E. S. Oran, and J. C. Wheeler. Deflagration-to-Detonation Transition in Thermonuclear Supernovae. *ApJ*, 478:678–+, March 1997.

M. Kuhlen, S. E. Woosley, and G. A. Glatzmaier. Carbon Ignition in Type Ia Supernovae. II. A Three-dimensional Numerical Model. *ApJ*, 640:407–416, March 2006. doi: 10.1086/500105.

J. Magnaudet and I Eames. The motion of high-reynolds-number bubbles in inhomogeneous flows. *Ann. Rev. Fluid Mech.*, 32:659–708, 2000.

D. W. Moore. The rise of a gas bubble in a viscous liquid. *J. Fluid Mech.*, 6:113–130, 1959.

J. C. Niemeyer and A. R. Kerstein. Burning regimes of nuclear flames in SN IA explosions. *New Astronomy*, 2:239–244, August 1997. doi: 10.1016/S1384-1076(97)00017-1.

J. C. Niemeyer and S. E. Woosley. The Thermonuclear Explosion of Chandrasekhar Mass White Dwarfs. *ApJ*, 475:740–+, February 1997.

J. C. Niemeyer, W. Hillebrandt, and S. E. Woosley. Off-Center Deflagrations in Chandrasekhar Mass Type IA Supernova Models. *ApJ*, 471:903–+, November 1996. doi: 10.1086/178017.

K. Nomoto, D. Sugimoto, and S. Neo. Carbon deflagration supernova, an alternative to carbon detonation. *Ap&SS*, 39:L37–L42, February 1976.

C. D. Ohl, A. Tijink, and A. Prosperetti. The added mass of an expanding bubble. *J. Fluid Mech.*, 482:271–290, 2003. doi: 10.1017/S002212003004117.

T. Plewa, A. C. Calder, and D. Q. Lamb. Type Ia Supernova Explosion: Gravitationally Confined Detonation. *ApJL*, 612:L37–L40, September 2004.

F. K. Röpke and W. Hillebrandt. Full-star type Ia supernova explosion models. *Astronomy and Astrophysics*, 431:635–645, February 2005.

K. Robinson, L. J. Dursi, P. M. Ricker, R. Rosner, A. C. Calder, M. Zingale, J. W. Truran, T. Linde, A. Caceres, B. Fryxell, K. Olson, K. Riley, A. Siegel, and N. Vladimirova. Morphology of Rising Hydrodynamic and Magnetohydrodynamic Bubbles from Numerical Simulations. *ApJ*, 601:621–643, February 2004. doi: 10.1086/380817.

F. K. Roepke, S. E. Woosley, and W. Hillebrandt. Off-center ignition in type Ia supernova: I. Initial evolution and implications for delayed detonation. *ArXiv Astrophysics e-prints*, 2006.

F. X. Timmes and F. D. Swesty. The Accuracy, Consistency, and Speed of an Electron-Positron Equation of State Based on Table Interpolation of the Helmholtz Free Energy. *ApJSS*, 126:501–516, February 2000.

F. X. Timmes and S. E. Woosley. The conductive propagation of nuclear flames. I - Degenerate C + O and O + Ne + Mg white dwarfs. *ApJ*, 396:649–667, September 1992.

Frank X. Timmes. The physical properties of laminar helium deflagrations. *Astrophysical Journal*, 528:913, 2000.

T. A. Weaver, G. B. Zimmerman, and S. E. Woosley. Presupernova evolution of massive stars. *ApJ*, 225:1021–1029, November 1978. doi: 10.1086/156569.

S. E. Woosley. Numerical simulations of burning. In *Talks at the Workshop on Classical Novae and Type Ia Supernovae, May 20-21, 2005, Santa Barbara, California*, 2005. <http://www.jinaweb.org/events/SB05/talks.html>.

S. E. Woosley. Models for type Ia supernovae. *Nuclear Physics A*, 688:9–16, May 2001. Nuclei in the Cosmos 2001.

S. E. Woosley, S. Wunsch, and M. Kuhlen. Carbon Ignition in Type Ia Supernovae: An Analytic Model. *ApJ*, 607:921–930, June 2004.

S. Wunsch and S. E. Woosley. Convection and Off-Center Ignition in Type Ia Supernovae. *ApJ*, 616:1102–1108, December 2004. doi: 10.1086/425116.

M. Zingale, S. E. Woosley, J. B. Bell, M. S. Day, and C. A. Rendleman. The physics of flames in Type Ia supernovae. *Journal of Physics Conference Series*, 16:405–409, January 2005a. doi: 10.1088/1742-6596/16/1/056.

M. Zingale, S. E. Woosley, C. A. Rendleman, M. S. Day, and J. B. Bell. Three-dimensional Numerical Simulations of Rayleigh-Taylor Unstable Flames in Type Ia Supernovae. *ApJ*, 632:1021–1034, October 2005b. doi: 10.1086/433164.

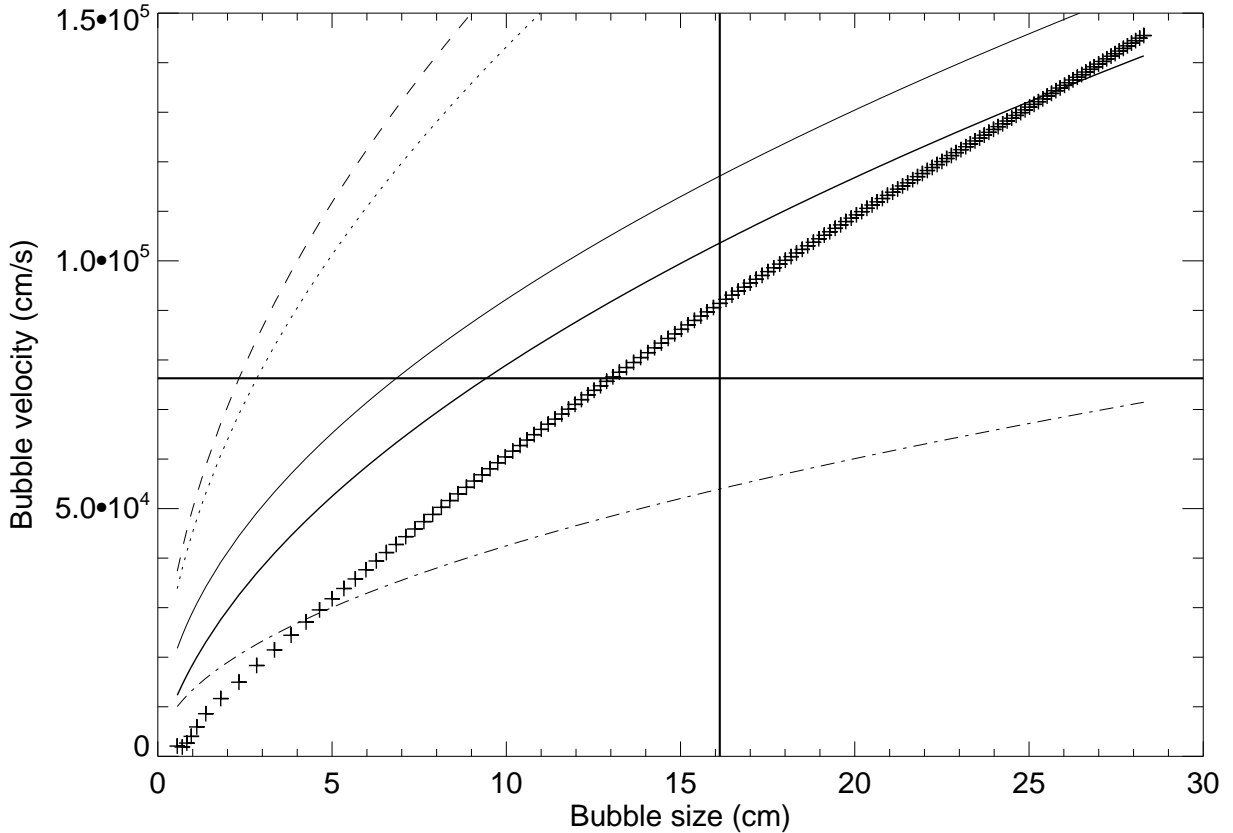


Fig. 1.— Different parameterizations of predicted rise velocity of a buoyant rigid spherical bubble (lines), for the specific case of a cylindrical flame burning into material of density $\rho = 4 \times 10^7 \text{ g cm}^{-3}$. Plus symbols represent simulation results described in §3. Lines are plotted for, top to bottom: dashed line – Davies-Taylor result, $v_{b,DT}$, Eq. 7; dotted line, same functional form, but with simple Atwood-number correction, $v_{b,DT+A}$, Eq. 9; thin solid line, rise velocity $v_{b,\text{rise}}$ from Eq. 10 but not taking into account flame expansion; solid line, rise velocity $v_{b,\text{rise}}$ from Eq. 10 taking into account flame expansion; dot-dashed line, Goncharov result $v_{b,RT}$ from Eq. 8 for Rayleigh-Taylor instability. All of these plots are for terminal velocities, so provide only an upper envelope for bubble speed. Horizontal line represents laminar planar flame speed, and vertical line indicates where buoyancy becomes dominant (here defined where the bottom of the bubble begins moving upwards) and so bubble begins deforming and these velocities no longer strictly apply.

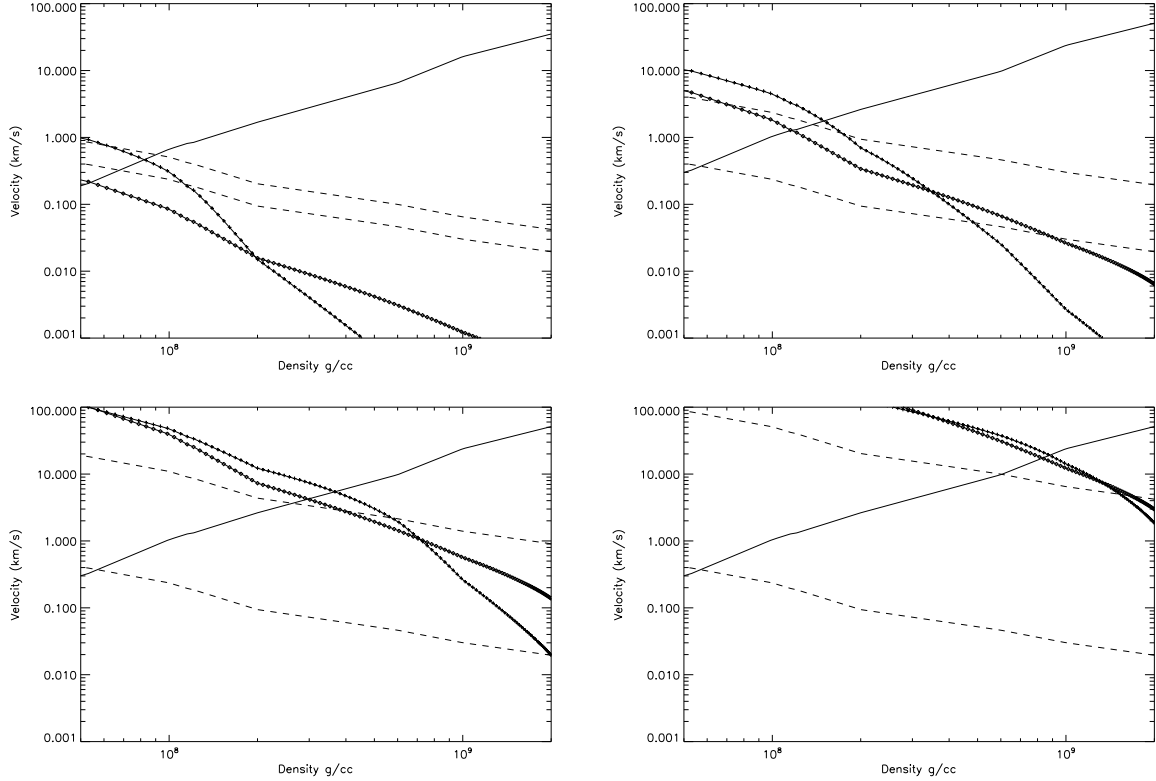


Fig. 2.— Velocities affecting the propagation of a flame bubble of given initial size at various densities in our white dwarf model. Plotted are the flame expansion velocity \dot{R} (solid line), fiducial turbulent velocities (dashed lines) assuming large-scale convective motions on 200km scales at $\approx 100\text{km s}^{-1}$; turbulent velocities are calculated on scales of the bubble ($v_{\text{turb},b}$, upper dashed line) and flame thickness ($v_{\text{turb},f}$, lower dashed line). Also plotted are terminal rise velocities of the flame bubble assuming the bubble rise speed is dominated by drag induced by the bubbles own motion ($v_{b,\text{rise}}$, + symbols) or determined by turbulent drag ($v_{b,\text{visc}}$, \diamond symbols). These quantities are plotted, left to right and top to bottom, for flame bubbles of size 5 , 5×10^2 , 5×10^4 , and 5×10^6 flame thicknesses at conditions corresponding to the given density. Buoyant and turbulent velocities are comparable because the origin of the large-scale turbulence is buoyant convection.

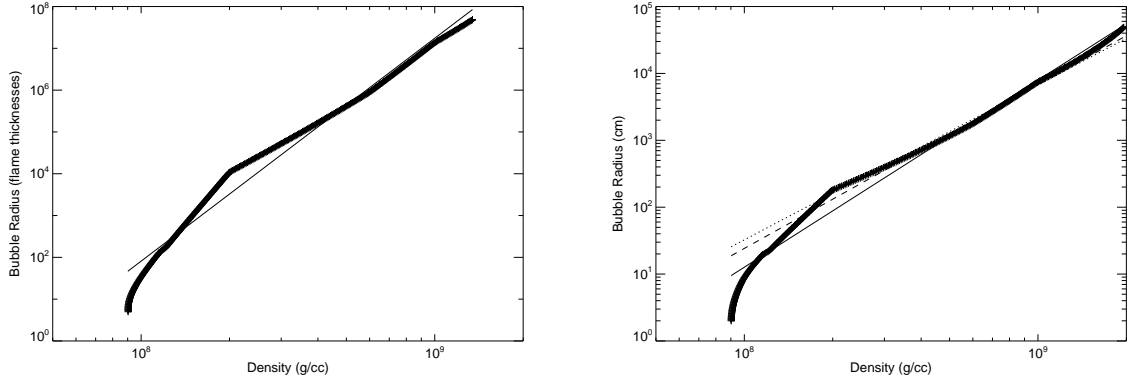


Fig. 3.— Plot in (ρ, r) space showing the size of a bubble r (on left, in local flame thicknesses; on right, in cm) where laminar flame speed dominates the other speeds calculated here, using same model as in Fig 2. Plus symbols indicate calculated values, and the solid line indicates fit values: on left $R = 81l_f \rho_8^{16/3}$, on right $R = 12.67\text{cm} \rho_8^{2.80}$. On the right is also plotted (the top solid line) the analytic approximation for the distortion radius for a turbulent rise velocity as given in Eq. 20 (dotted) and that for the laminar rise velocity (dashed).

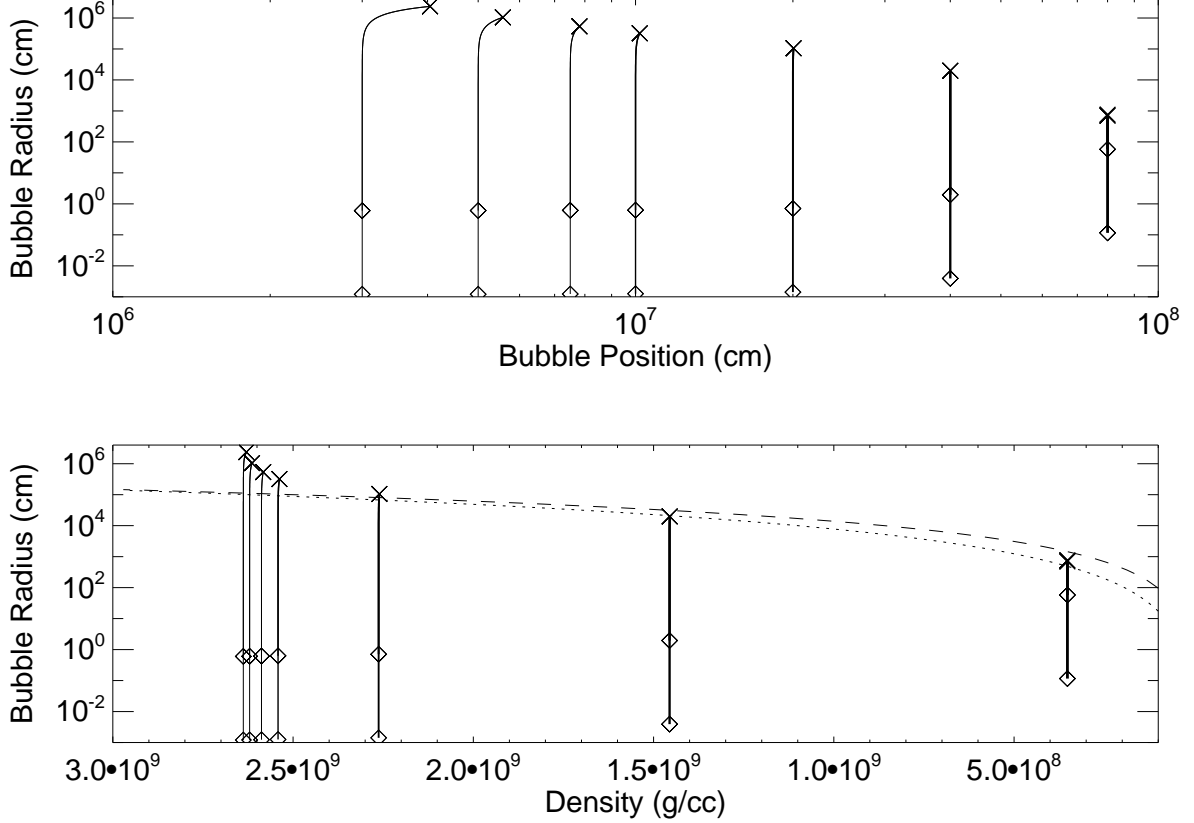


Fig. 4.— Semi-analytic evolution of flame bubble sizes and positions, shown as trajectories in (R, r) and (ρ, r) space, with flame bubbles of varying sizes and initial positions. The top panel shows the evolution of bubble radius r and position from the center of the white dwarf R ; the bottom panel shows position in terms of density ρ . Trajectories are evolved from the initial conditions (\diamond) until the flame velocity no longer dominates and evolution becomes turbulent and fragmentation of the bubble becomes possible (marked by 'X'). Varying thickness of the lines denote different initial conditions, with lines of the same thickness in each panel indicating evolution of the same bubble in the different plots. Because by definition we are only considering times where while buoyant rise velocities are small compared to flame velocities, the position and ambient density change little during the course of the evolution, although at very high densities where the flame speed is quite high more rising can occur. The bubbles are initially set to be 10 and 5000 flame thicknesses in radius; as this figure shows, the only difference in evolution in these cases is where along the trajectory the flame bubble begins. On the bottom panel, the dotted line indicates the simple fit for the critical bubble size as a function of density, as plotted in Fig 3, and the dashed line indicates the analytic approximation given in Eq. 20.

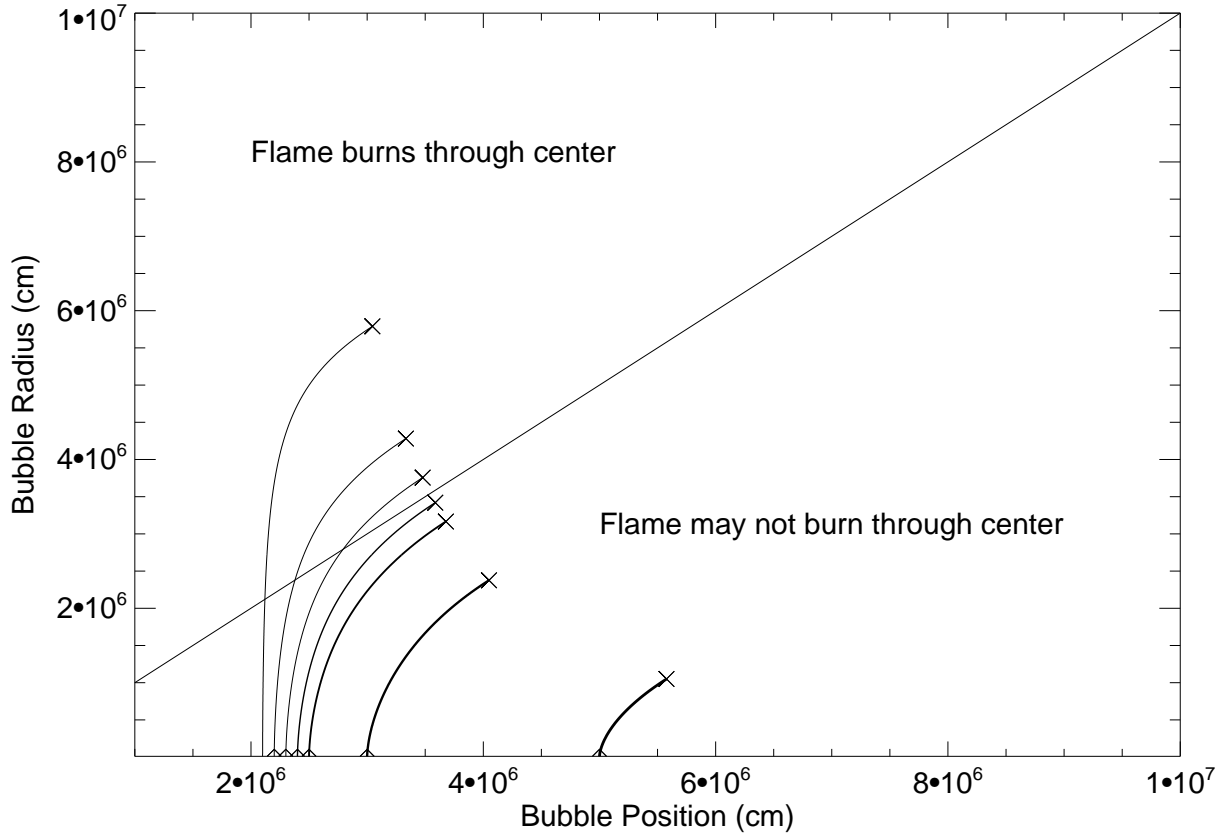


Fig. 5.— Semi-analytic evolution of flame bubble sizes and positions, as in Fig. 4, but focused on bubbles which start very near the center – plotted are trajectories of bubbles with initial positions, left to right, of 21, 22, 23, 24, 25, 30, and 50 km – and the end of the trajectories. Those bubbles whose final size before distortion by turbulence or buoyancy exceed their radial positions certainly and immediately burn through the center of the star, and thus do not leave a central region of fuel behind. The first bubble whose final size does not exceed their radial position sets the maximum size of a bubble which does not burn through the center, because of the downward and monotonic relationship between density and final size as shown in Fig. 3. For the white dwarf progenitor considered here, bubbles beginning at positions closer than ≈ 23.5 km to the center of the star will burn through the center, while those at a larger distance, while burning to a radius of ≈ 30 km before other effects take hold, will not.

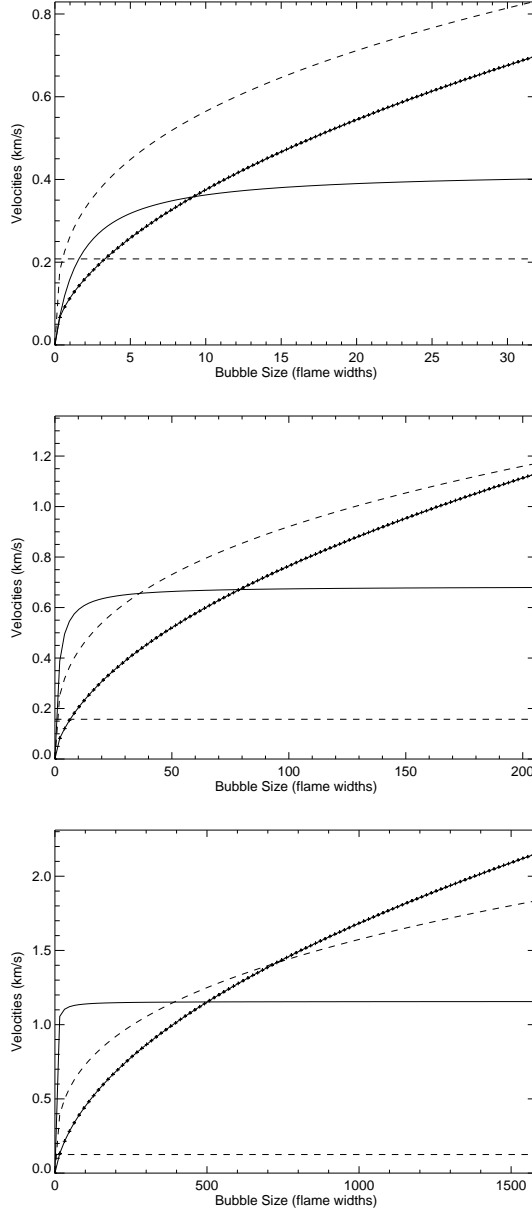


Fig. 6.— Plot of predicted velocities for a flame bubble burning a 50/50 mixture by mass of Carbon and Oxygen, using the simplified $^{12}\text{C} + ^{12}\text{C} \rightarrow ^{24}\text{Mg}$ burning network, for comparison with numerical results. Shown are quantities at density $\rho = 2.35 \times 10^7 \text{ g cm}^{-3}$, (top) with a flame thickness of 0.18 cm, $\rho = 3 \times 10^7 \text{ g cm}^{-3}$, (middle) with a flame thickness of 0.078 cm, and $\rho = 4 \times 10^7 \text{ g cm}^{-3}$ (bottom) with flame thickness of 0.039 cm. Gravity is fixed at $g = 10^{10} \text{ cm s}^{-2}$. The solid line shows laminar flame velocity, plus signs indicate terminal bubble rise velocity, and dashed lines indicate turbulent velocities on bubble (top) and flame (bottom) scales assuming motions of 100 km s^{-1} on an integral scale of 200 km . Terminal bubble speed is plotted assuming a quiescent medium, *e.g.* drag is due to the bubbles motions only.

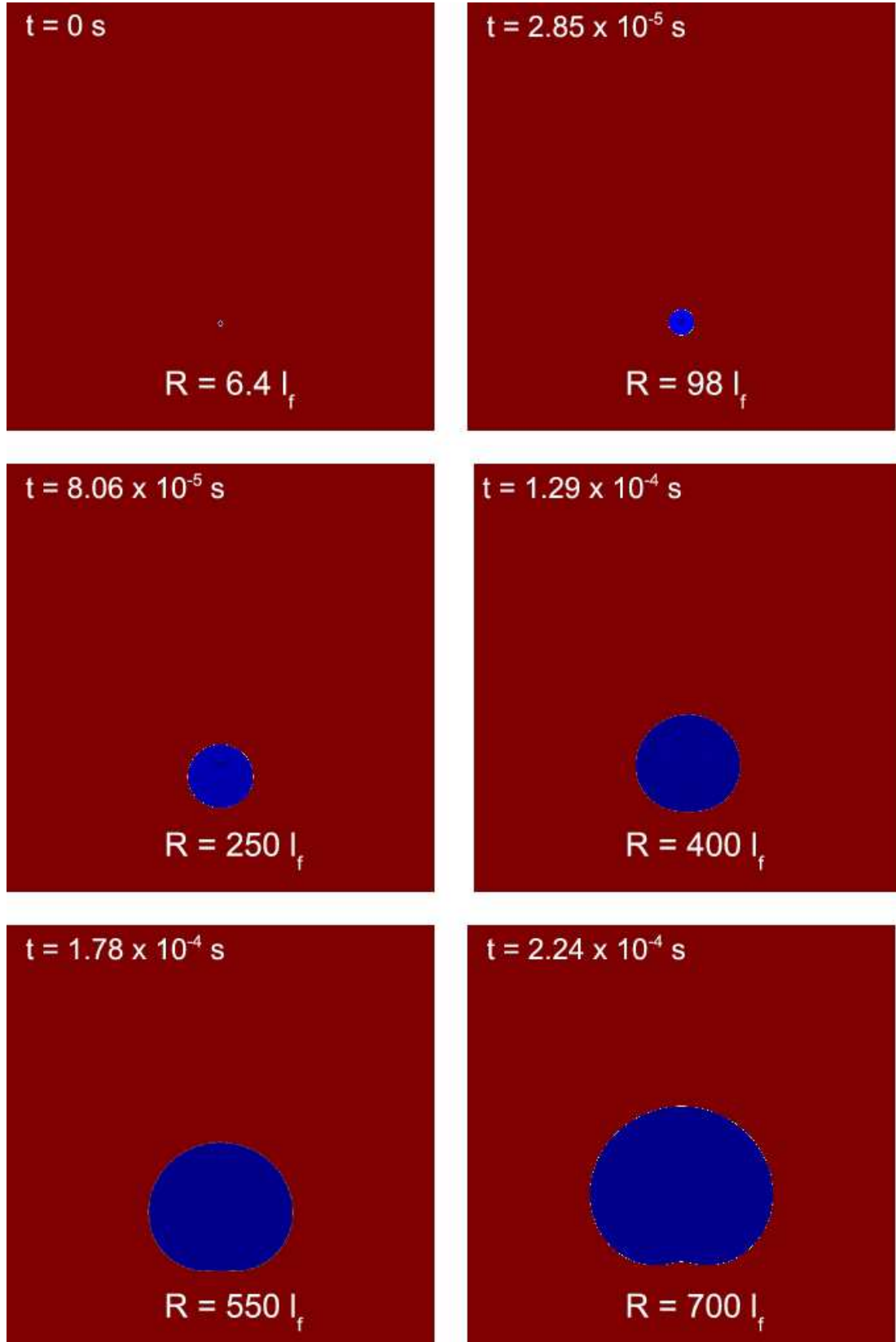


Fig. 7.— Evolution of a $4 \times 10^7 \text{ g cm}^{-3}$ flame bubble. The bubble burns out in a circular fashion until it reaches about 400 thermal thicknesses in radius. At this point, it begins to deform. Only the lower half the computational domain is shown here.

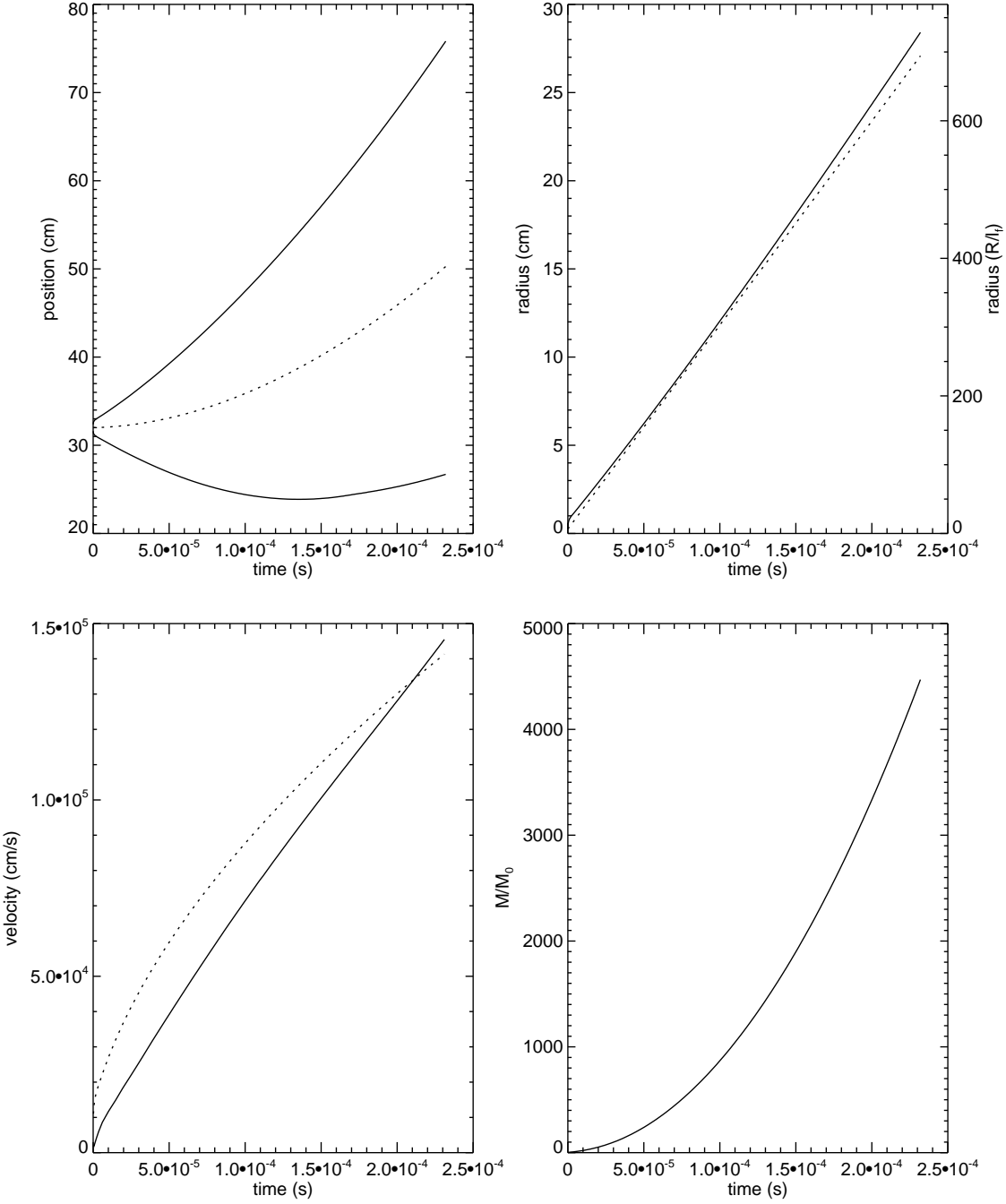


Fig. 8.— Bubble position, size, rise velocity, and mass as a function of time for the $4 \times 10^7 \text{ g cm}^{-3}$ flame bubble. In the top left panel, positions are shown for top and bottom of the bubble (solid lines) and center of mass of the bubble (dashed line). In the top right panel, radius is plotted, in both centimeters and flame thicknesses, with the solid line being the measured size and the dashed line given by Eq. 3. In the bottom left, the bubble rise velocity is plotted as measured (solid line) and as given by Eq. 10 (dashed). On the bottom right panel is shown the burned mass inside the bubble.

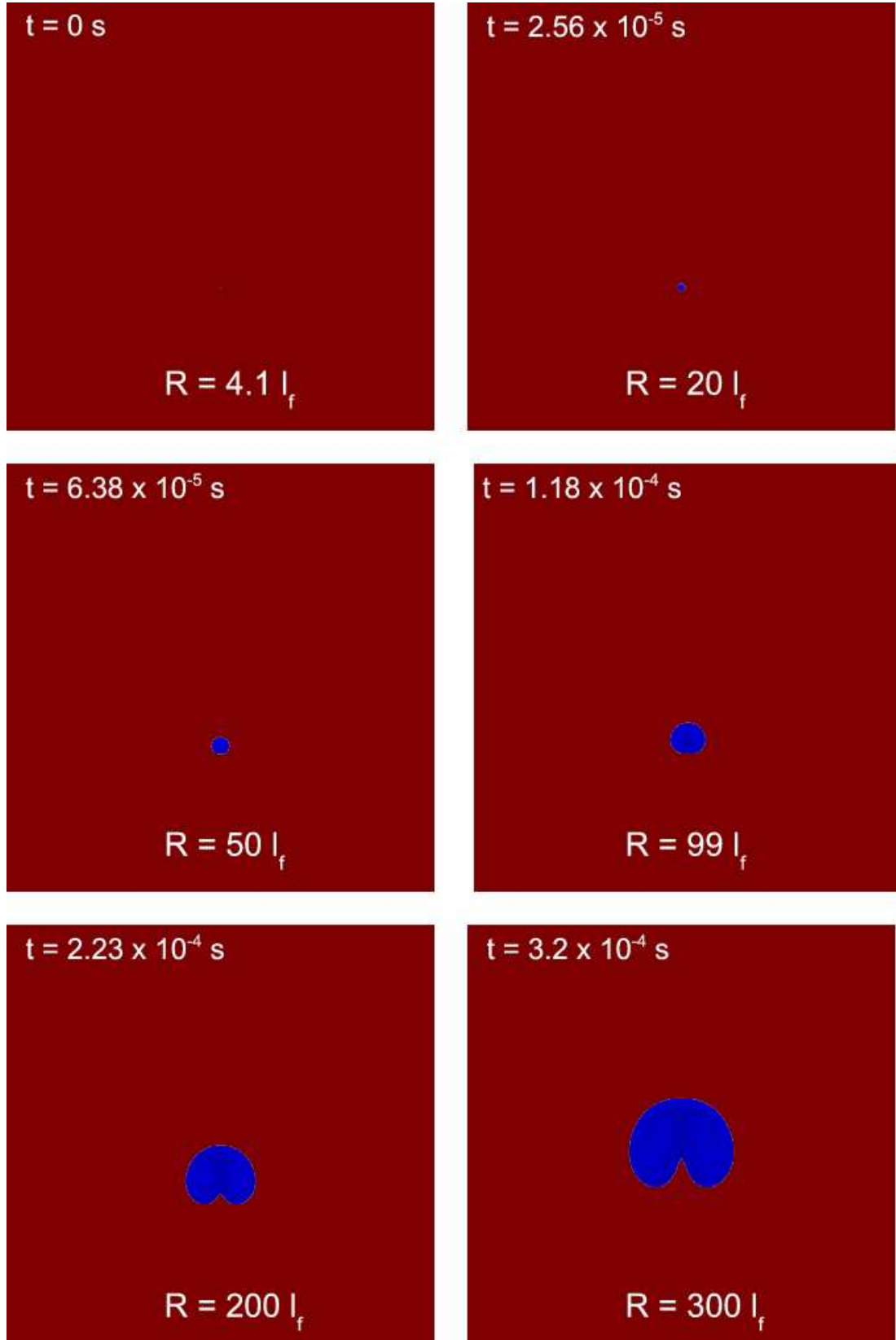


Fig. 9.— Evolution of a $3 \times 10^7 \text{ g cm}^{-3}$ flame bubble. The bubble burns out in a circular fashion until it reaches about 100 thermal thicknesses in radius. At this point, it begins to deform. Only the lower portion of the computational domain is shown here.

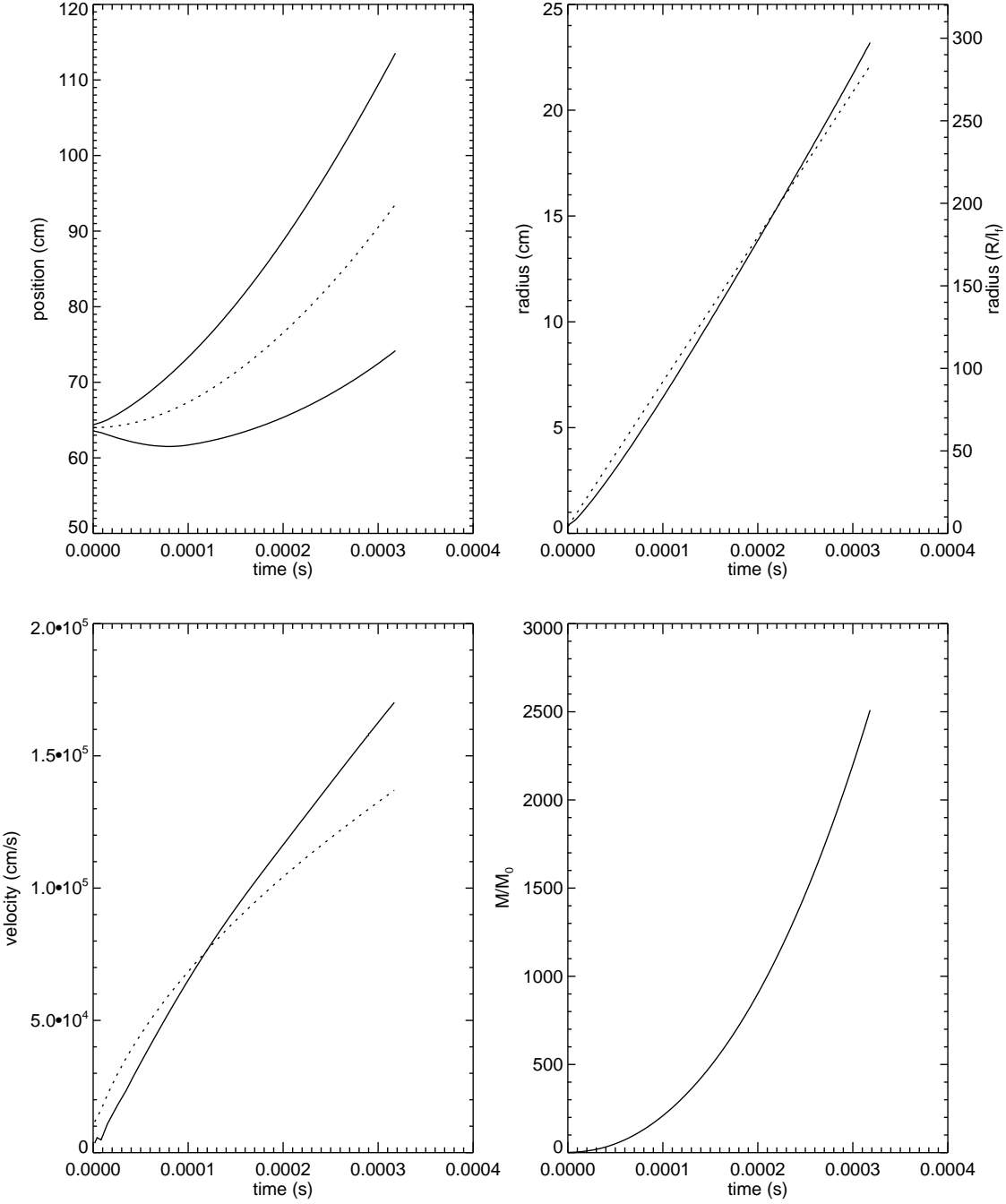


Fig. 10.— Bubble position, size, rise velocity, and mass as a function of time for the $3 \times 10^7 \text{ g cm}^{-3}$ flame bubble. In the top left panel, positions are shown for top and bottom of the bubble (solid lines) and center of mass of the bubble (dashed line). In the top right panel, radius is plotted, in both centimeters and flame thicknesses, with the solid line being the measured size and the dashed line given by Eq. 3. In the bottom left, the bubble rise velocity is plotted as measured (solid line) and as given by Eq. 10 (dashed). On the bottom right panel is shown the burned mass inside the bubble.

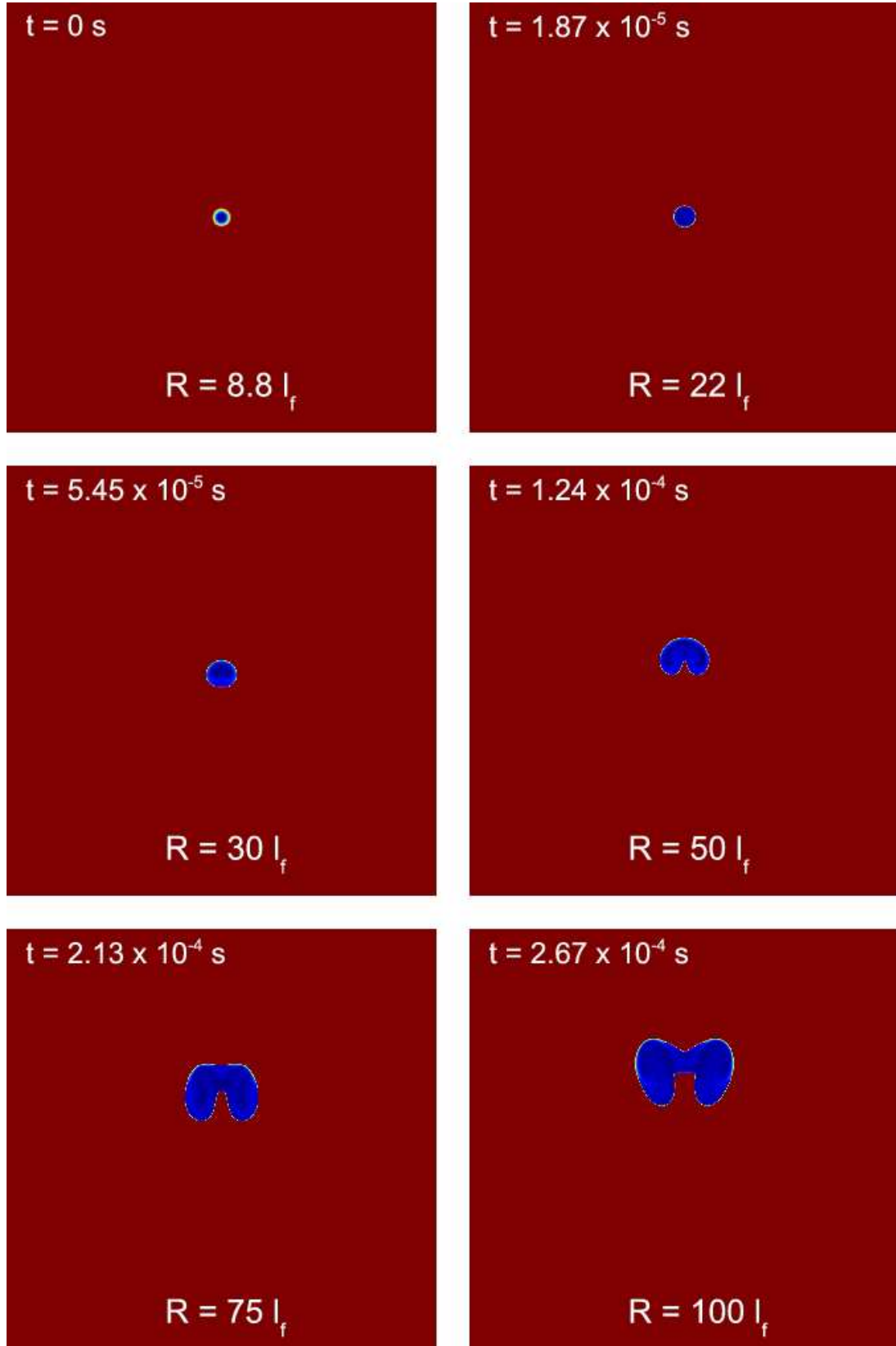


Fig. 11.— Evolution of a $2.35 \times 10^7 \text{ g cm}^{-3}$ flame bubble. In contrast to Figure 7, the lower density bubble begins to deform at a much smaller radius. Only a portion of the computational domain is shown here.

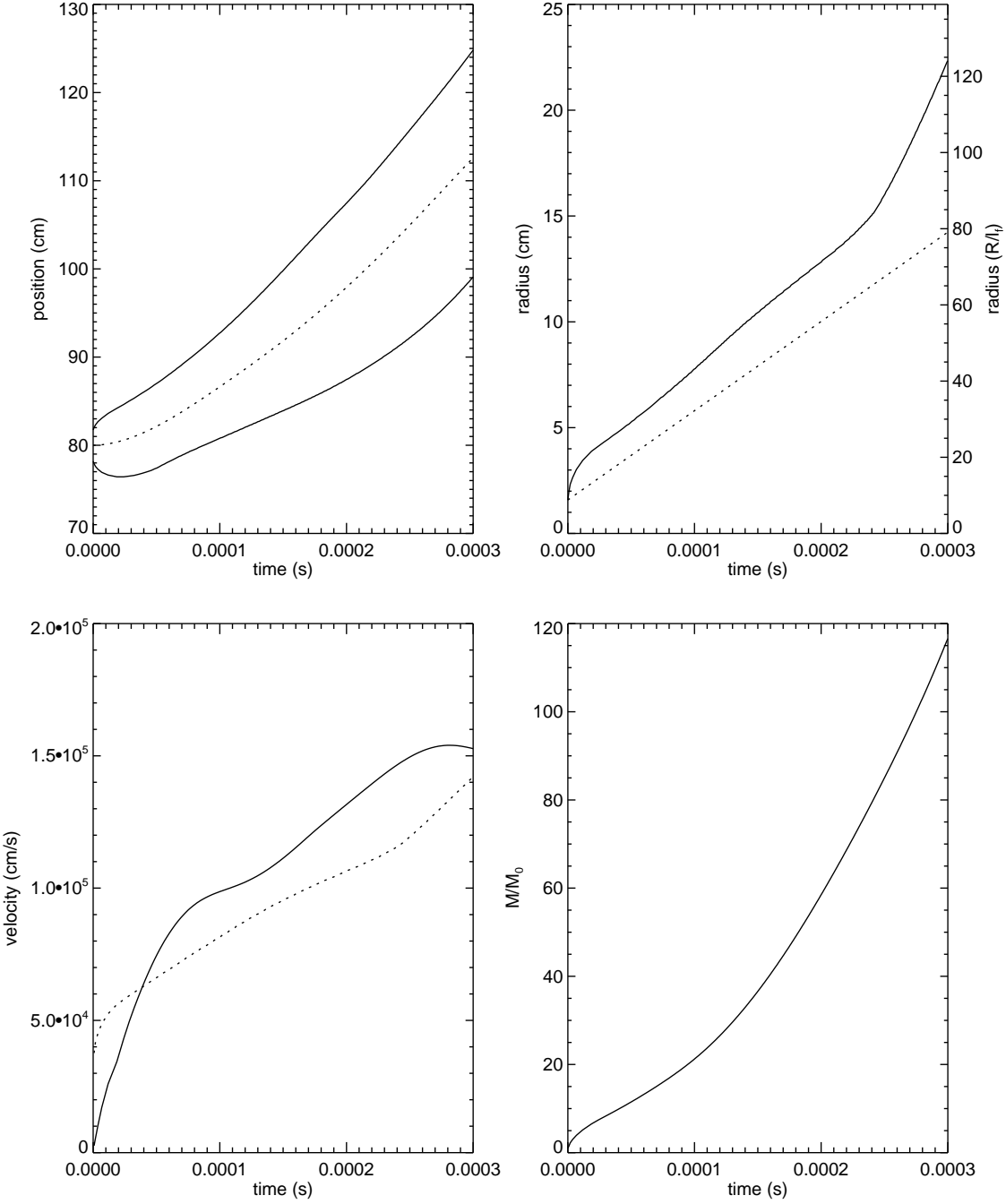


Fig. 12.— Bubble position, size, rise velocity, and mass as a function of time for the $2.35 \times 10^7 \text{ g cm}^{-3}$ flame bubble. In the top left panel, positions are shown for top and bottom of the bubble (solid lines) and center of mass of the bubble (dashed line). In the top right panel, radius is plotted, in both centimeters and flame thicknesses, with the solid line being the measured size and the dashed line given by Eq. 3. In the bottom left, the bubble rise velocity is plotted as measured (solid line) and as given by Eq. 10 (dashed). On the bottom right panel is shown the burned mass inside the bubble.

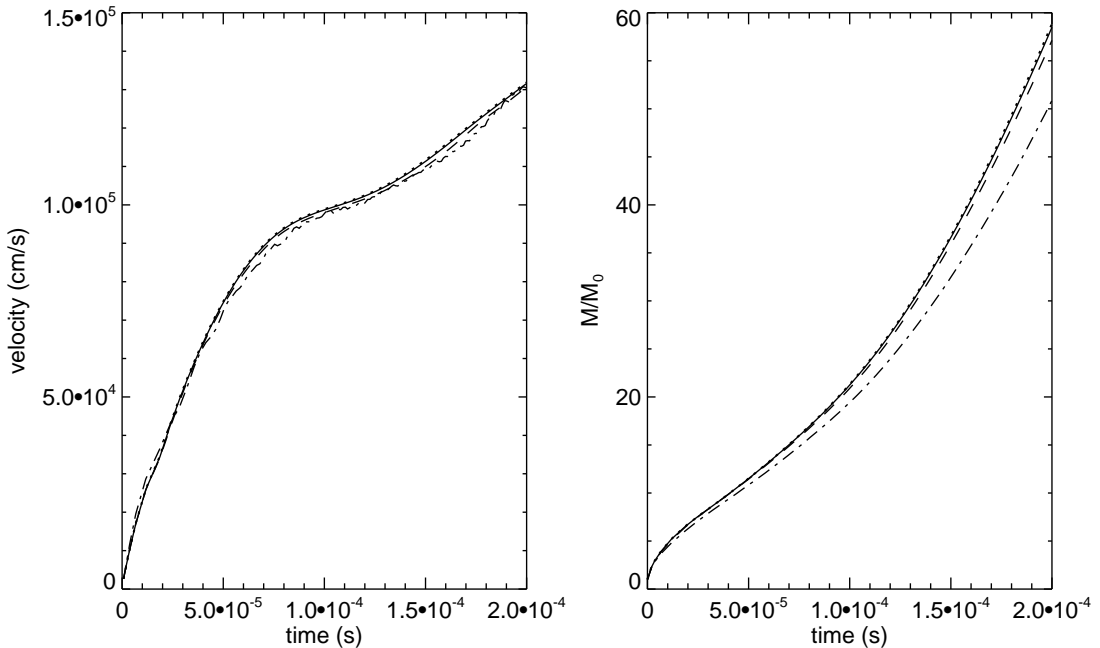


Fig. 13.— Bubble radius and rise velocity as a function of time for the $2.35 \times 10^7 \text{ g cm}^{-3}$ bubble, with simulations run at four different resolution. The solid line represents results using the resolution used in the present analysis (4.6 zones / l_f), the dotted line is a higher resolution run (9.2 zones / l_f), the dashed line is a low resolution run (2.3 zones / l_f), and the dot-dash line is at a lowest resolution (1.15 zones / l_f). The fiducial- and high-resolution curves lie nearly on top of one another, demonstrating that our simulation is converged. Significant divergence of the very low resolution run in the mass plot is seen—evidence that at this lowest resolution, we are incompletely resolving the burning, although the large-scale rising dynamics is robust even at this very low resolution.

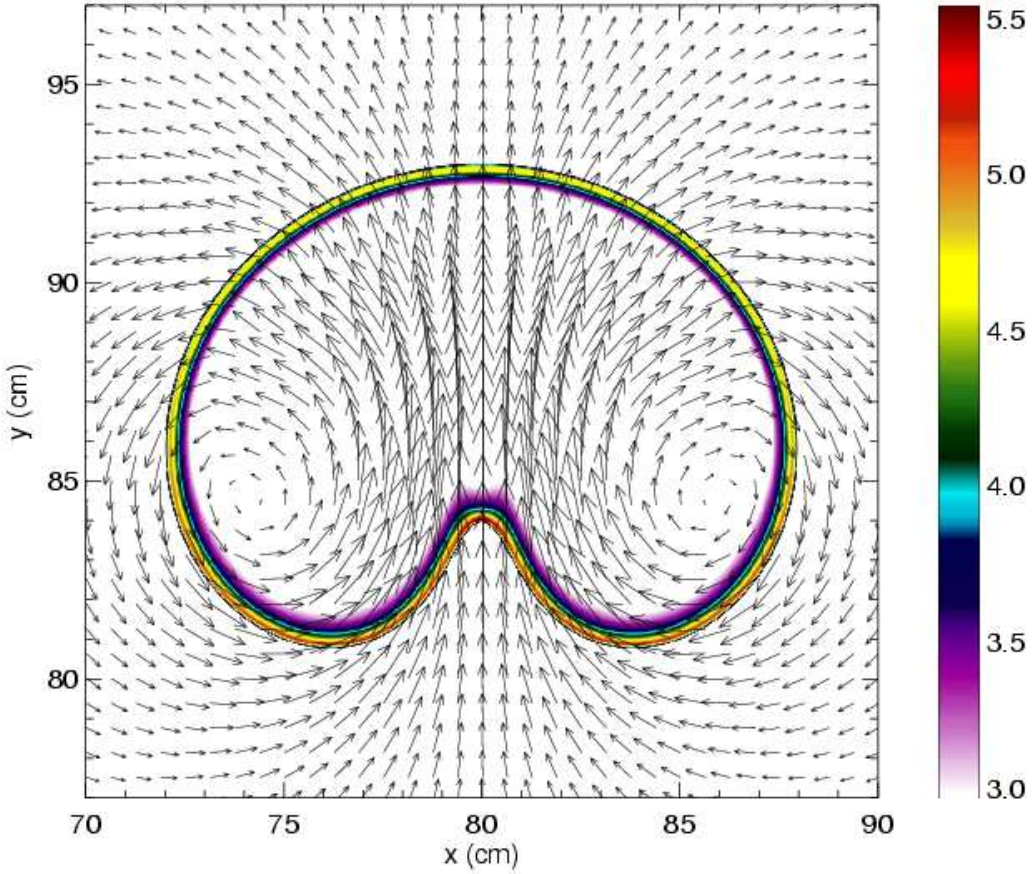


Fig. 14.— Base-ten logarithm of the carbon destruction rate ($-dX(^{12}\text{C})/dt$) for the $2.35 \times 10^7 \text{ g cm}^{-3}$ bubble at 10^{-4} s , after the deformation has begun. For reference, a planar laminar flame has a peak destruction rate of $1.3 \times 10^5 \text{ s}^{-1}$, or $\log_{10}(-dX(^{12}\text{C})/dt) = 5.1$. Notice that the most vigorous burning occurs on the bottom of the bubble, with an intensity approximately twice that of an unstrained laminar flame.